frontiers in Earth Science

ORIGINAL RESEARCH
published: 18 March 2021
doi: 10.3389/feart.2021.635178

Soil Degassing From the Xianshuihe–Xiaojiang Fault System at the Eastern Boundary of the Chuan–Dian Rhombic Block, Southwest China

Yutao Sun[1,2], Xiaocheng Zhou[3], Yucong Yan[3], Jingchao Li[3], Wenya Fang[3], Wanli Wang[3] and Yongmei Liu[4]*

[1]Hebei Key Laboratory of Strategic Critical Mineral Resources, Hebei GEO University, Shijiazhuang, China, [2]College of Earth Sciences, Heibei GEO University, Hebei Province, Shijiazhuang, China, [3]Institute of Earthquake Forecasting, China Earthquake Administration, Beijing, China, [4]Seismological Bureau of Inner Mongolia Autonomous Region, Hohhot, China

OPEN ACCESS

Edited by:
Francesco Italiano, National Institute of Geophysics and Volcanology, Italy

Reviewed by:
Alessandra Sciarra, Istituto Nazionale di Geofisica e Vulcanologia (INGV), Italy
Galip, Yuce, Hacettepe University, Turkey

***Correspondence:**
Xiaocheng Zhou
zhouxiaocheng188@163.com

Specialty section:
This article was submitted to Structural Geology and Tectonics, a section of the journal Frontiers in Earth Science

Received: *30 November 2020*
Accepted: *21 January 2021*
Published: *18 March 2021*

Citation:
Sun Y, Zhou X, Yan Y, Li J, Fang W, Wang W and Liu Y (2021) Soil Degassing From the Xianshuihe–Xiaojiang Fault System at the Eastern Boundary of the Chuan–Dian Rhombic Block, Southwest China. Front. Earth Sci. 9:635178. doi: 10.3389/feart.2021.635178

The Chuan–Dian region, situated in the middle part of the north-south seismic zone of mainland China in a highly deformed area of the eastern margin of the Tibetan Plateau, is one of the principal areas for monitoring earthquake activities in China. In this study, the geochemical characteristics of soil degassing (of CH_4, H_2, CO_2, Rn, and Hg) and, the relationship between degassing and fault activity, were investigated in the Xianshuihe–Xiaojiang fault system (XXFS) at the eastern boundary of the Chuan–Dian rhombic block. The mean soil-gas concentrations of CH_4, H_2, CO_2, Rn, and Hg in the XXFS were 8.1 ppm, 9.9 ppm, 0.5%, 15.1 kBq/m^3 and 12.9 ng/m^3, respectively. The $\delta^{13}C_{CO2}$ and $\delta^{13}C_{CH4}$ values of the hot-spring gases varied from –11.9‰ to –3.7‰ and –62.5‰ to 17‰, respectively. The He-C isotopic ratios indicate that the carbon in the northern and middle parts of the XXFS may have originated from deep fluids, whereas the carbon in the southern part of the XXFS is of organic origin. The high concentrations of soil gas were distributed near the faults, indicating that the faults could act as channels for gas migration. The distributions of the high soil-gas concentrations in the XXFS coincide with the highest stress and maximum strain rates, indicating that the fault activity enhanced permeability and increased the emission rates of the gases. The results of this study will be helpful for degassing in active fault zones and earthquake monitoring.

Keywords: soil gas, CO_2, CH_4, H_2, Rn, Hg

INTRODUCTION

Degassing (of gases such as Rn, He, CO_2, CH_4, CO, H_2, N_2, and Hg) from the solid Earth to the atmosphere can be enhanced by varying the crustal stress (King, 1986; Toutain and Baubron, 1999; Du et al., 2008; Bohnhoff and Zokack, 2010). Previous studies and field observations have demonstrated that faults and/or fractures are highly permeable pathways for gas migration from gas sources, which retain the signatures of gas sources in the soil cover (e.g. Fu et al., 2005; Ciotoli et al., 2014, 2016; Sciarra et al., 2015, 2017, 2018, 2020; Yuce et al., 2017; Xiang et al., 2020). Gas anomalies are well-correlated with earthquakes (e.g. King, 1986; Du et al., 2008; Einarsson et al.,

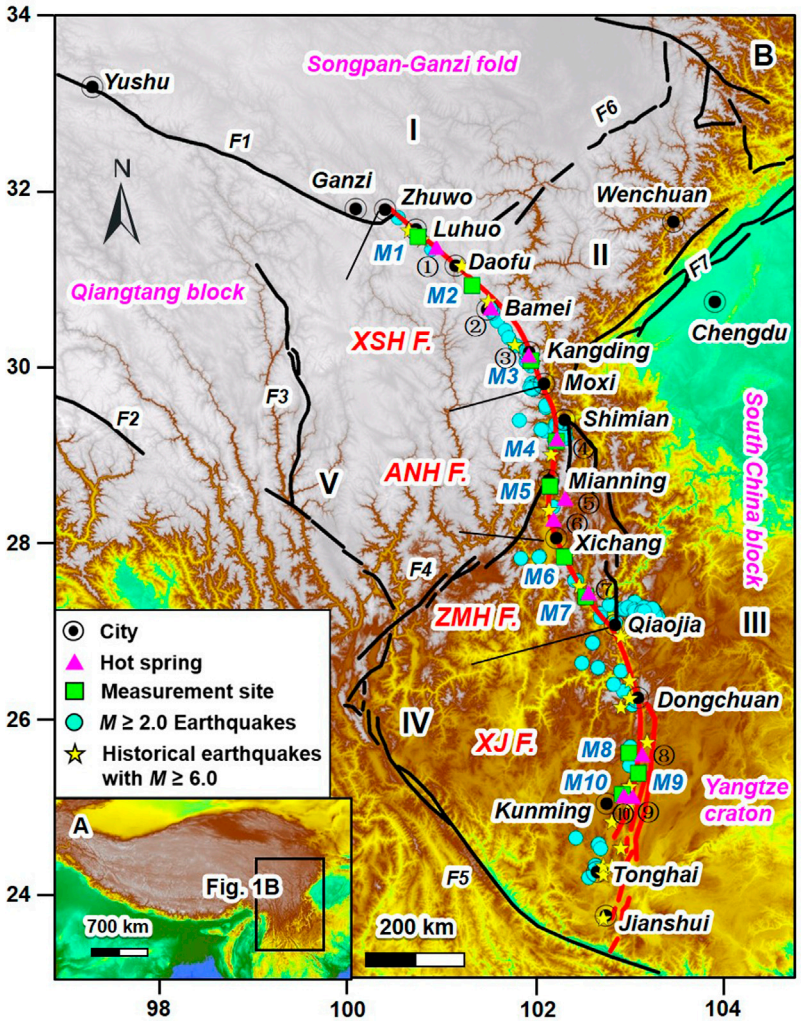

FIGURE 1 | (A) Geological map showing the location of the study area. **(B)** Tectonic and topographic map in the Chuan–Dian rhombic block. I, Ahba block; II, Longmenshan block; III, south China block; IV, the southern subblock of the Chuan–Dian terrace; V, the northern subblock of the Chuan–Dian terrane. F1, Ganzi-Yushu fault; F2, Jiali fault; F3, Jinshajiang fault; F4, Xiaojinhe fault; F5, Red River fault; F6, Longriba fault; F7, Longmenshan fault zone. Modified after Jiang et al. (2014). M1-M10 are the soil-gas measurement sites in this study. Abbreviations of the faults: XSH, Xianshuihe fault; ANH, Anninghe fault; ZMH, Zemuhe fault; XJ, Xiaojiang fault. Numbers ①–⑩ represent the bubbling hot springs distributed along the XXFS (Kama, Guanding, Zimakua, Xide, Hongmo, Liutie, Xundiantang, Yiliang, and Tangchi hot springs, respectively). The $M \geq 2.0$ earthquakes occurred from January 2012 to October 2020 within 50 km of the XXFS. Earthquake data are from China Earthquake Networks Center (CENE, http://www.ceic.ac.cn). Data of the histotical earthquakes are from Wang et al. (2008) and Wen et al. (2011).

2008; Li et al., 2009) and are much more sensitive to stress variations (King, 1986; Einarsson et al., 2008; Toutain and Baubron, 1999). Therefore, soil-gas measurement is an efficient tool for the study of fault activity (e.g. Toutain and Baubron, 1999; Walia et al., 2010; Yang et al., 2011).

Northward subduction of the Indian plate beneath the Tibetan Plateau makes south-eastern Tibet an important domain involved in the convergence and interaction between the Eurasian and Indian plates (**Figure 1A**, Tapponnier et al., 2001). The Chuan–Dian region, in the southern part of the north-south seismic zone of mainland China, is tectonically located in the highly deformed area of the eastern Tibetan Plateau. Enclosed by the Xianshuihe–Xiaojiang fault system (XXFS), the Red River fault, and the Jinshajiang fault (**Figure 1B**), the Chuan–Dian rhombic block is one of the principal areas of earthquake monitoring in China.

The XXFS is located at the eastern boundary of the Chuan–Dian rhombic block (**Figure 1B**) and has a curved left-lateral strike-slip structure extending at least 1,400 km into the eastern margin of the Tibetan Plateau (Allen et al., 1991). Fieldwork confirms that the XXFS is one of the largest and most seismically active fault systems in China. The XXFS has experienced at least 35 earthquakes of $M > 6$ in the last 300 years, and almost all segments of the system have been the locus of major earthquakes within the historical record (BGMRSP, 1993; **Figure 1B**).

Previous studies primarily focused on the soil gas and hot-spring gas at the western boundary of the Chuan–Dian rhombic

block (e.g. Li et al., 2018; Zhou et al., 2020). However, at the eastern boundary of the rhombic block, only the geochemical characteristics of several gas species (CO_2, Rn, and Hg) in the middle part of the XXFS have been reported (Zhang et al., 2019a; Zhange, 2019b). So far, systematic investigation of multi-gas components in soil gases at the eastern boundary of the rhombic block has rarely been reported. In this study, the geochemical characteristics of soil degassing of CH_4, H_2, CO_2, Rn, and Hg and the relationship between degassing and fault activity in the XXFS were reported.

GEOLOGICAL SETTING

The XXFS consists of the Xianshuihe (XSH), Anninghe (ANH), Zemuhe (ZMH), and Xiaojiang (XJ) faults from north to south (**Figure 1B**).

The NW-striking XSH fault is a highly active strike-slip fault in the eastern margin of the Tibetan Plateau that begins in Luding, passes through Kangding and Luhuo, and extends into Qinghai Province (**Figure 1B**). The XSH fault has a long active history. The regional uplift tectonic motion of the Tibetan Plateau in the Neogene produced the XSH NW–NNW striking left-lateral slip fault that cuts through the sialsphere, producing the belts of intensive faults and cleavage. The XSH fault is very active and is accompanied by many destructive earthquakes, such as the M = 7.9 earthquake that occurred in Luhuo in 1973 (**Figure 1B**, BGMRSP, 1993).

The ANH fault starts from the town of Jintang, passes through Mianning, Dechang, and Huili, and extends into Yunnan Province. The ANH fault is multi-segmented. The northern, middle, and southern segments are separated at Shimian and Dechang. In this study, the northern and middle segments of the ANH fault were selected for targeting. The northern segment of the ANH fault is characterized by thrust and ductile shear, whereas the middle segment is characterized by deep faulting. Seismic activities in these segments are severe, with many $M \geq 6$ earthquakes occurring (BGMRSP, 1993).

The ZMH NW-striking fault conjoins with the ANH fault at Xichang and is currently active (BGMRSP, 1993). The basement of the ZMH fault primarily consists of metamorphic rocks derived from granite, rhyolite, and basalt (Ren et al., 2010). Quaternary alluvial sediments, which are primarily composed of sandy gravel, fine sand, silt, and clay, are widely distributed in the study area (Ren et al., 2010).

The XJ fault is a zone of intense seismic activity that starts from Zhaojue in Sichuan Province and terminates in Yunnan Province. The fault divides into two branches south of the city of Dongchuan (**Figure 1B**). A wide crushed zone formed along the fault. The XJ fault is distinctly currently active and is characterized by frequent seismic activities and many hot springs (BGMRSP, 1993).

The field survey showed hot springs widely distributed along the XXFS (Zhou et al., 2015). In this study, the Jinkagu (①), Kama (②), and Guanding (③) hot springs in the XSH fault; the Zimakua (④), Xide (⑤), and Hongmo (⑥) hot springs in the ANH fault; the Liutie (⑦) hot spring in the ZMH fault; and the Xundian (⑧), Yiliang (⑨), and Tangi (⑩) hot springs in the XJ fault (**Figure 1B**) are distributed near the soil-gas measurement sites (**Figure 1B**); bubbling gas from these hot springs was sampled.

MEASUREMENT AND SAMPLING METHOD

Measurement Method of Soil Gas

The soil-gas measurements in the XXFS were conducted on 1–13 March 2019 to minimize the effect of weather factors. Ten

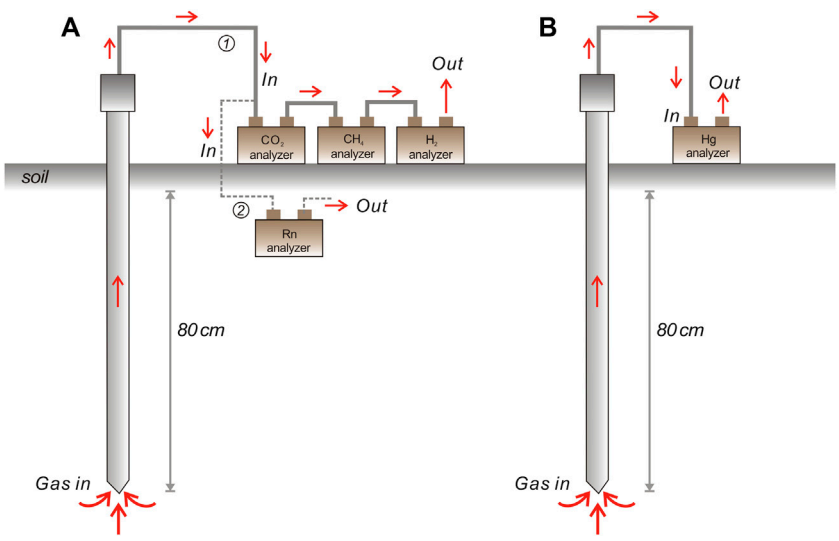

FIGURE 2 | Sketch map showing the measurement method of soil gases in the XXFS. ① and ② represent the first and second steps of the measurement at S1. Details of the measurement method can be found in the text.

TABLE 1 | Soil-gas concentrations at each measurement site in the XXFS.

Measurement site	Fault	CH_4 (ppm)		H_2 (ppm)		CO_2 (%)		Rn (kBq/m^3)		Hg (ng/m^3)	
		Min	Max	Min	Max	Min	Max	Min	Max	Min	Max
M1	XSH	0.8	31.4	0.3	59.1	0.02	2	2.3	258	5	18
M2	XSH	0.5	13.4	0.3	52.9	0.01	2.53	4.2	32.7	7	22
M3	XSH	0	9.2	0.2	43.5	0.03	1.56	1.1	52.6	7	26
M4	ANH	0	25.8	0.2	174.8	0.03	1.14	2.1	15.6	9	21
M5	ANH	0	180	0.2	96.1	0.04	1.05	0.2	43.1	4	50
M6	ZMH	0.8	97.4	0.2	193.3	0.08	1.04	0.9	26.1	7	63
M7	ZMH	0	1,130	0.2	22.7	0.02	0.82	1.1	28.4	4	19
M8	XJ	0	2.9	0.2	1.6	0.05	1.54	2.6	90.8	5	36
M9	XJ	0	7.3	0.2	19	0.18	25	1.1	43.5	4	32
M10	XJ	0	2.5	0.2	2.6	0.26	2.24	0.03	53.8	1	78

measurement sites (M1 to M10 in **Figure 1B**) along the XXFS were selected for measurement. The measurement sites of M1–M3, M4–M5, M6–M7, and M8–M10 were in the XSH, ANH, ZMH, and XJ faults, respectively (**Figure 1B**). M8 and M10 were in the western branch of the XJ fault, whereas M9 was in the eastern branch of the XJ fault (**Figure 1B**).

Four parallel survey lines with an interval of approximately 10 m were laid across the fault at each measurement site. Gas concentrations were measured at 16 points on each survey line; 72 measurement points at M3 were laid out across the XSH fault. The distance between each measurement point was approximately 10 m, whereas those far from the fault were separated by approximately 20–100 m at places that were confined by local conditions. A total of 648 soil-gas measurement points for each gas species were measured in the XXFS.

The measurement method of the soil-gas concentration was the same as that reported by Zhou et al. (2016). Before measurement, two samplers (S1 and S2), 1-m in length and 2.3-cm in diameter, were hammered into the soil at a depth of ~80 cm (**Figure 2**). The concentrations of soil gas at a depth of ~80 cm were measured. The distance between the two samplers was 50 cm. S1 was used to measure CO_2, CH_4, H_2, and Rn concentrations. The CO_2 analyser was connected to S1 to first measure the CO_2 concentration. The CH_4 analyser was connected to the outlet of the CO_2 analyser, and the H_2 analyser was connected to the outlet of the CH_4 analyser (**Figure 2A**). When the measurements of CO_2, CH_4, and H_2 concentrations were finished, the Rn analyser was connected to S1 for the measurement (**Figure 2A**). S2 was only used to measure Hg concentration (**Figure 2B**).

The CO_2 concentration was measured using the non-dispersive infrared gas analyser GXH-3010 with a measuring resolution and accuracy of 0.001% and 4%, respectively (Zhou et al., 2016). The concentration of CH_4 was measured using the Huberg LASER ONE with a measurement resolution and accuracy of 1 ppm and 5%, respectively. The concentration of H_2 in the soil gas was measured using the ATG-300H analyser, which has been widely used for the measurement of fault degassing. The measurement range and resolution of the H_2 analyser were 0–5,000 ppm and 0.1 ppm, respectively. An RAD7 Radon Detector and an RA-915+ Zeeman Mercury Analyser were used to measure Rn and Hg concentrations in soil gas, respectively.

Sampling and Analyzing Methods of Hot-Spring Gas

Ten bubbling hot-spring gas samples were collected from the hot springs of ①–⑩ in the XXFS (**Figure 1B**) in 2017 and 2018 using the water displacing method. The gases were collected in soda-lime glass bottles with a volume of 500 ml. An inverted funnel was submerged and placed on top of the bubbles to collect the hot-spring gas. The collected gas in the funnel flowed into a bottle

TABLE 2 | Threshold values, proportions, mean concentration of each population, and 95% confidence interval of soil gases in the XXFS obtained by statistical approach.

Gas species	Number of measurement point	LAT[a]	UAT[a]	Proportion (%)			Mean gas concentration of each population			Mean gas concentration	95% confidence interval
				A[b]	B[b]	C[b]	A[b]	B[b]	C[b]		
CH_4 (ppm)	648	1.6	8.1	24.4	54.8	20.8	1.1	2.8	72.3	8.1	4.1–12.9
H_2 (ppm)	648	2.0	47.7	30.4	61.3	8.3	0.5	13.5	77.7	9.9	8.3–11.4
CO_2 (%)	648	0.2	0.7	54.0	40.7	5.2	0.1	0.4	1.3	0.5	0.4–0.6
Rn (kBq/m^3)	648	2.3	24.9	2.2	84.9	13.0	1.2	11.8	38.4	15.1	13.9–16.1
Hg (ng/m^3)	648	5.0	29.0	4.9	93.1	2.0	3.2	12.8	42.5	12.9	12.4–13.4

[a]*LAT, lower anomaly threshold; UAT, upper anomaly threshold.*

[b]*The A, B and C are the three populations identified by the thresholds. See details in the text.*

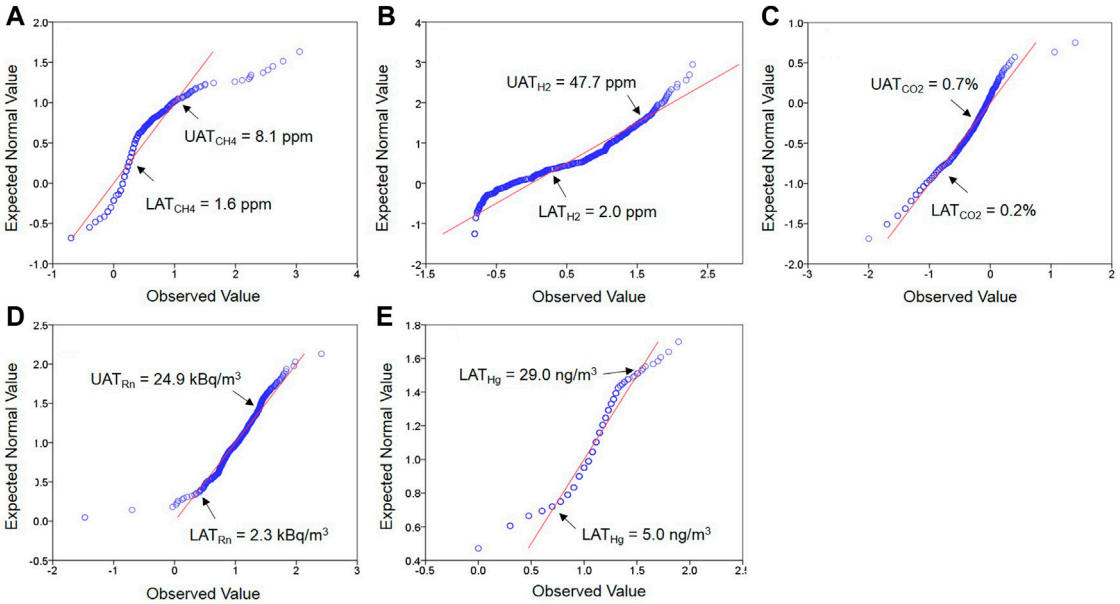

FIGURE 3 | Normal probability plots for: **(A)**, CH_4; **(B)**, H_2; **(C)**, CO_2; **(D)**, Rn; **(E)**, Hg.

filled with hot-spring water and replaced the water in the bottle (Zhou et al., 2015; Zhang et al., 2017). Details of the sampling method can be found in Zhou et al. (2015) and Zhang et al. (2017).

The $\delta^{13}C_{CO2}$ and $\delta^{13}C_{CH4}$ values of the gas samples were analysed at the Key Laboratory of Petroleum Resources Research, Institute of Geology and Geophysics, Chinese Academy of Science. A GC-IRMS analytical system gas chromatograph (Agilent 6890)-stable isotope ratio mass spectrometer (Thermo-Fisher Scientific Delta Plus XP) was used for carbon isotopic ratio analysis. The $\delta^{13}C_{CO2}$ and $\delta^{13}C_{CH4}$ values were reported relative to PDB.

RESULTS AND DISCUSSION

Statistical Results and Spatial Distributions of Soil Gases in the XXFS

The statistical results of the CH_4, H_2, CO_2, Rn, and Hg concentrations at each measurement site are listed in **Table 1**. The concentrations of CH_4, H_2, CO_2, Rn, and Hg in the XXFS range from 0–1,130 ppm, 0.2–193.3 ppm, 0.01–25%, 0.03–258 kBq/m^3, and 1–78 ng/m^3, respectively (**Table 1**).

We used the normal probability method proposed by Sinclair (1991) to objectively identify the threshold, which distinguishes different populations (background, mixing, and anomalous) well (e.g. Sinclair, 1974, 1991; Sciarra et al., 2015, 2017, 2018, 2020; Zhou et al., 2015; Yuce et al., 2017). The background population is related to surface processes, such as soil respiration, air dilution, and biological gas origin. The anomaly population is primarily related to internal processes, such as fault/magma degassing (e.g. Chiodini et al., 2004; Sciarra et al., 2015, 2017, Sciarra, 2018, Sciarra, 2020; Di Martino et al., 2016; Yuce et al., 2017). The mixing population represents soil gas with mixing sources by external and internal processes (e.g. Yuce et al., 2017).

The lower anomaly thresholds (LAT) of CH_4, H_2, CO_2, Rn, and Hg in the XXFS were 1.6 ppm, 2.0 ppm, 0.2%, 2.3 kBq/m^3, and 5.0 ng/m^3, respectively (**Figure 3** and **Table 2**). The upper anomaly thresholds (UAT) of CH_4, H_2, CO_2, Rn, and Hg were 8.1 ppm, 47.7 ppm, 0.7%, 24.9 kBq/m^3, and 29.0 ng/m^3, respectively (**Figure 3** and **Table 2**). Accordingly, the data of each soil-gas species in the XXFS could be divided into the background (A), mixing (B), and anomaly (C) populations. The proportion and mean concentrations of each population of CH_4, H_2, CO_2, Rn, and Hg in the XXFS are listed in **Table 2**. The mean concentration of each gas species was calculated using **Eq. 1** (Sinclair, 1974):

$$P_M = f_A P_A + f_B P_B + f_C P_C \quad (1)$$

where P_M is the mean concentration of each gas species; f_A, f_B and f_C are the proportion of each population, and P_A, P_B, and P_C are

TABLE 3 | The $\delta^{13}C_{CO2}$ and $\delta^{13}C_{CH4}$ values of bubbling hot-spring gases in the XXFS.

No	Hot springs	Fault	Sampling date	Temp (°C)	$\delta^{13}C_{CH4}$ (‰, vs. PDB)	$\delta^{13}C_{CO2}$ (‰, vs. PDB)
①	Jinkagu	XSH	2017-7-17	16.5	n.d	−3.7
②	Kama	XSH	2017-7-13	32.0	−21.0	−5.2
③	Guanding	XSH	2017-7-6	75.8	−27.9	−6.0
④	Zimakua	ANH	2018-6-17	14.0	n.d	−5.9
⑤	Xide	ANH	2015-7-18	39.7	−49.0	−9.7
⑥	Hongmo	ANH	2017-1-7	49.2	17.0	−9.5
⑦	Liutie	ZMH	2017-1-8	57.9	−62.5	−6.7
⑧	Xundiantang	XJ	2017-1-10	58.2	−20.6	−4.1
⑨	Yiliang	XJ	2018-3-11	51.0	n.d	−11.9
⑩	Tangchi	XJ	2018-3-11	72.0	n.d	−6.9

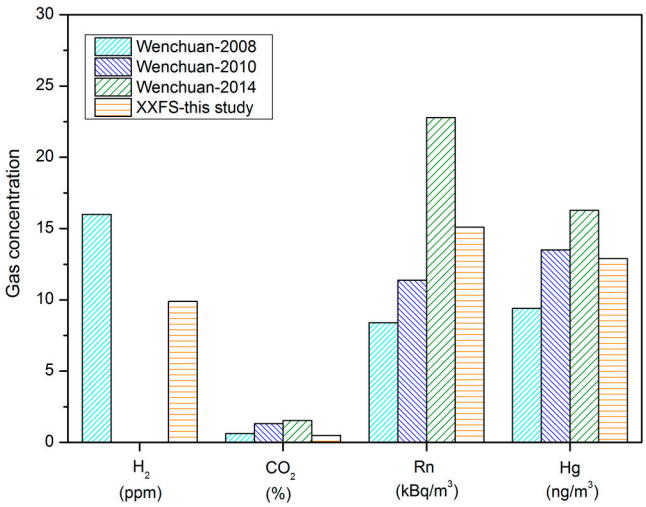

FIGURE 4 | Comparations of H_2, CO_2, Rn, and Hg concentrations in the XXFS and the surface rupture zone produced by the Wenchuan *Ms* 8.0 earthquake. Data sources: Zhou et al. (2010); Zhou et al. (2015); Zhou et al. (2016).

the mean gas concentrations of each population. Therefore, the mean concentrations of CH_4, H_2, CO_2, Rn, and Hg in the XXFS were calculated to be 8.1 ppm, 9.9 ppm, 0.5%, 15.1 kBq/m^3, and 12.9 ng/m^3, respectively (**Table 2**), which were close to the soil-gas concentrations measured in the surface rupture zone produced by the Wenchuan *Ms* 8.0 earthquake in 2008 and 2010 (**Figure 4**, Zhou et al., 2010; Zhou, et al., 2017).

The spatial distributions of soil-gas concentrations at the 10 measurement sites (obtained by using Kriging interpolation) are shown in **Figure 5**. From the spatial distributions of each gas species, high concentrations of soil gas were spatially coincident with the location of the fault and appeared close to the fault (**Figure 5**).

Origin of Carbon in the CO_2 and CH_4

Gas emissions from the fault zones are from multiple sources (e.g. Williams-Jones et al., 2000; Hong et al., 2010). Mantle, metamorphism of carbonate-bearing rocks, decomposition of organic material and surface biological activity are the principal sources of CO_2 in active fault zones (Irwin and Barnes, 1980; Toutain and Baubron, 1999), whereas microbiological and thermogenic genesis are the major processes of CH_4 genesis (e.g. Toutain and Baubron, 1999; Milkov and Etiope, 2018).

In this study, the $\delta^{13}C_{CO2}$ and $\delta^{13}C_{CH4}$ values of the hot-spring gas samples varied from -11.9‰ to -3.7‰ and -62.5‰ to 17‰, respectively (**Table 3**), and are consistent with the $\delta^{13}C_{CO2}$ and $\delta^{13}C_{CH4}$ values reported in previous studies (**Figure 6A**; Zhou et al., 2015; Shen et al., 2007). Combined with the carbon isotopic values reported in previous studies, the $\delta^{13}C_{CO2}$ and $\delta^{13}C_{CH4}$ values in the XXFS varied from -21.37‰ to -2.9‰ and -62.5‰ to 19‰, respectively (**Figure 6A** and **Supplementary Table S1**; Zhou et al., 2015; Shen et al., 2007).

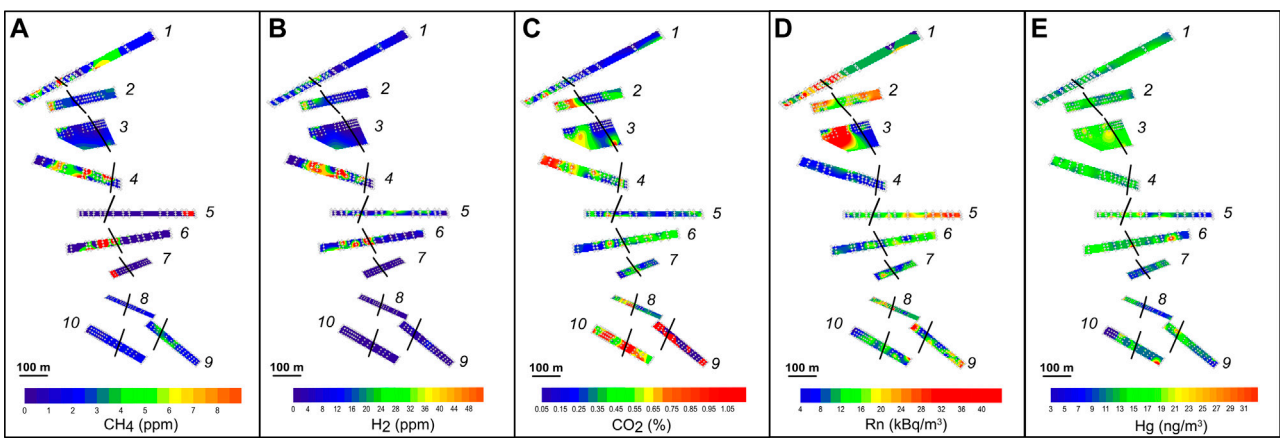

FIGURE 5 | Spatial distribution of soil-gas concentrations from M1–M10 in the XXFS. The white cross shows the distribution of the measurement points.

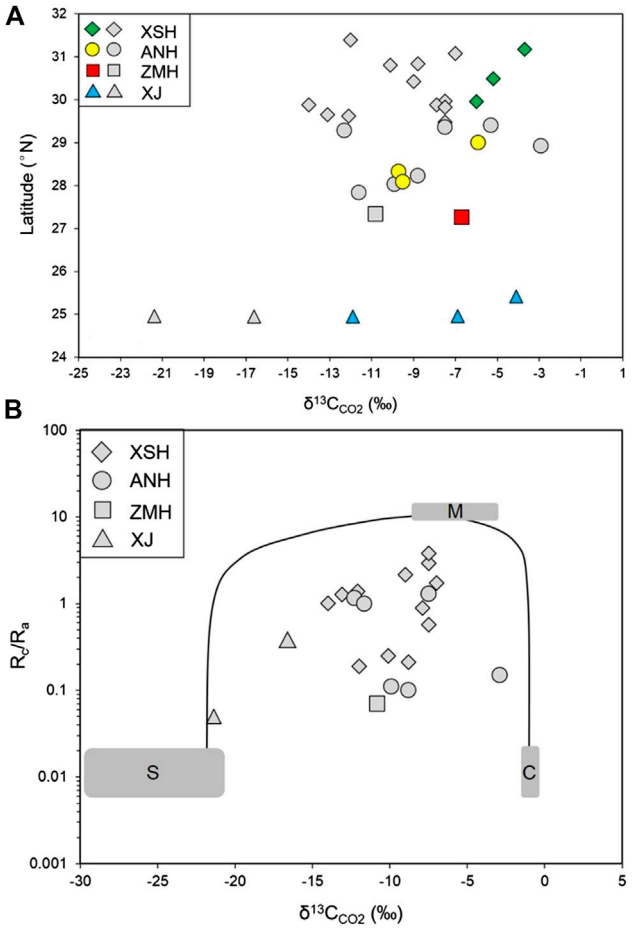

FIGURE 6 | (A) Plot of the $\delta^{13}C_{CO2}$ values from south to north along the XXFS. **(B)** R_c/R_a *vs.* $\delta^{13}C_{CO2}$ plot showing mixing of the end-members of mantle (M), crust (C), and sediment (S) of the bubbling gas samples in the XXFS. The colour symbols are data from bubbling hot-spring gas in this study. The grey symbols are hot-spring gas data reported in Shen et al. (2007) and Zhou et al. (2015). The He-C isotopic data in June 2009 were selected in this study in consideration of the significant influence of earthquake on the variations of He-C isotopic ratios (Zhou et al., 2015).

Previous studies indicated that upper mantle-derived CO_2 has $\delta^{13}C_{CO2}$ values between −3‰ and −9‰ with an average value of −6.5‰ (Javoy et al., 1986; Marty and Jambon, 1987). Soil organic matter derived from C3 and C4 plants have $\delta^{13}C_{CO2}$ values varying from −12‰ to −14‰ and −24‰ to −27‰, respectively (Cheng, 1996). The R_c/R_a-$\delta^{13}C_{CO2}$ plot reveals that the gas samples in the XXFS show characteristics of mixing among the end-members of the mantle, crust, and sediment (**Figure 6B**). However, the He-C isotopic ratios in the XSH and ANH faults showed obvious characteristics of mixing between the end-members of the mantle and crust, whereas those in the ZMH and XJ faults showed greater addition of organic sources (**Figure 6B**). The $\delta^{13}C_{CO2}$ values near M9 and M10 in the XJ fault are −21.37‰ to −6.9‰ (**Table 3** and **Supplementary Table S1**; Shen et al., 2007), with majority of the $\delta^{13}C_{CO2}$ values within the domain of organic carbon source.

The spatial distributions of the CO_2 concentration in the XXFS show that the highest concentrations of CO_2 were found at M9 and M10 in the XJ fault (**Figure 5C**). Therefore it could deduce that the carbon in the XJ fault in southern part of the XXFS has an organic carbon source.

CH_4 of microbial origin usually has $\delta^{13}C_{CH4}$ values < -55‰, whereas $\delta^{13}C_{CH4}$ values of thermogenic origin vary from −30‰ to −50‰ (Milkov and Etiope, 2018 and references therein). Abiotic CH_4 is ^{13}C-enriched with $\delta^{13}C_{CH4}$ values > −20‰ (Milkov and Etiope, 2018 and references therein). The $\delta^{13}C_{CH4}$-$\delta^{13}C_{CO2}$ diagram shows that the majority of the gas samples in the XXFS are plotted within the thermogenic and abiotic domains (**Figure 7**), indicating the mixing sources of CH_4 in the XXFS.

Geophysical studies (e.g. Liu and Wang, 2020) indicate that anomalies of low velocity and high Poisson's ratio are present at the XSH, ANH, and ZMH faults in the XXFS (26.5° N, 28° N, 29.5° N, 31.5° N, **Figure 1B** and Liu and Wang, 2020) and are interpreted as fluid intrusions (partial melt of deep material) from the lower crust and/or uppermost mantle. The $\delta^{13}C_{CO2}$ values in the XSH, ANH, and ZMH faults are higher than those in the XJ fault (**Figure 8A**; **Table 3** and **Supplementary Table S1**). According to previous studies, the $^3He/^4He$ ratios in the XXFS are 0.05–3.8 R_a (where R_a is the air-corrected $^3He/^4He$ ratios, **Supplementary Table S1**; Shen et al., 2007; Zhou et al., 2015), which lie within the typical crust and mantle domains (e.g. Sano and Marty, 1995; Zhang et al., 2017). The $^3He/^4He$ ratios in the XSH, ANH, and ZMH faults range from 0.19 to 3.8 R_a, 0.1–1.3 R_a, and 0.07 R_a, respectively, which are higher than those in the XJ fault (0.05–0.35 R_a) (**Figure 8B** and **Supplementary Table S1**). Analysis of He-C isotopic ratios in the XXFS was used to deduce that the carbon in the XSH, ANH, and ZMH faults might have originated from deep fluids, whereas the carbon in the XJ fault is of organic origin.

Anomaly and Degassing of Rn in the XXFS

Rn is inert and has low mobility in the geological environment (Tanner, 1964; Dubois et al., 1995). The uranium decay and the upward migration of Rn along the fault could represent the two sources of Rn in the fault zone (Toutain and Baubron, 1999; Sciarra et al., 2015; Sciarra et al., 2017; Sciarra et al., 2018; Sciarra et al., 2020). Previous studies indicate that the emanating power of the rock and soil, the permeability of the host rock, and the flow of the carrying gas are the primary factors that influence Rn activity in a diffusive system (e.g. Ball et al., 1991; Morawska and Phillips, 1993). Therefore, we used the formula of Åkerblom (1993) (**Eq. 2**), which is based on the ^{222}Rn activity at equilibrium with parent radionuclides (radium) in the soil, by verifying the anomaly threshold to determine the origin of Rn in the XXFS (Åkerblom, 1993; Sciarra et al., 2018):

$$C_{Rn} = C_{Ra}\varepsilon\rho n^{-1} \quad (2)$$

where C_{Rn} and C_{Ra} are the concentrations of Rn and radium in the soil gas (Bq/m^3) and soil (Bq/kg), respectively. ε is the emanation power coefficient (non-dimensional), ρ is the soil density (kg/m^3), and n is the effective porosity coefficient (non-dimensional).

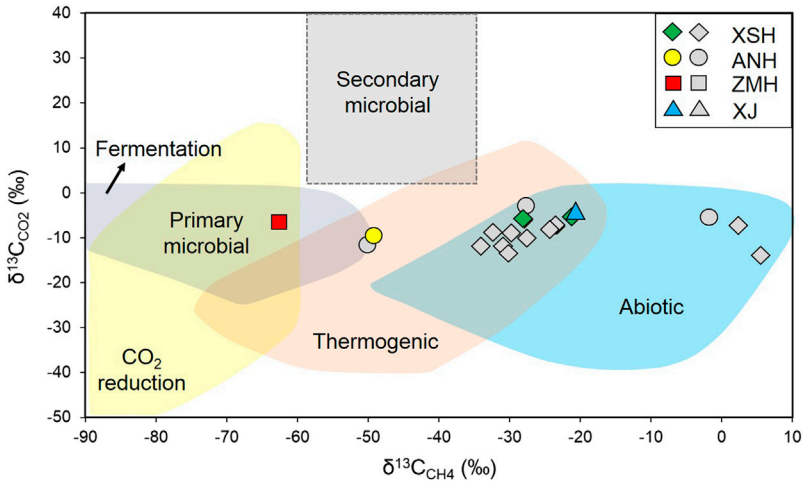

FIGURE 7 | Plot of $\delta^{13}C_{CO2}$ *vs.* $\delta^{13}C_{CH4}$. The colour symbols are data from bubbling hot-spring gas in this study. The grey symbols are hot-spring gas data reported in Shen et al. (2007) and Zhou et al. (2015). Modified after Milkov and Etiope (2018).

Previous studies show that the average content of soil radium-226 in China is 36.5 Bq/kg (e.g. Sun et al., 2004). The ε values are variable in different rock and soil types (e.g. Righi and Bruzzi, 2006; Jobbágy et al., 2009; Qin, 2012; Shen et al., 2012). The surrounding rocks and strata outcrop in the XXFS can be divided into four types: 1) volcanic rocks and acidic intrusions; 2) dolomite, limestone and carbonate; 3) sandstone; and 4) polyterrigenous materials (**Table 4**, BGMRSP, 1993). Therefore, the ε values of the four types of surrounding rocks and strata in the XXFS have values of 0.48 (Qin, 2012), 0.074 (Righi and Bruzzi, 2006; Jobbágy et al., 2009), 0.4 (Qin, 2012), and 0.12 (Shen et al., 2012), respectively (**Table 5**). The values of the soil porosity (n) were calculated using **Eq. (3)**:

$$n = 1 - (\text{subsoil bulk density}/2.65) \quad (3)$$

where 2.65 g/cm^3 is the mean density of soil porosity. The values of subsoil bulk density (kg/m^3) at a depth of 100 cm in the XXFS were selected from the Harmonized World Soil database (HWSD), which is elaborated by the Food and Agriculture Organization (FAO) (FAO/IIASA/ISRIC/ISSCAS/JRC, 2012). Therefore, the calculated Rn concentrations from M1–M10 in the XXFS ranged from 8.5 kBq/m^3 to 61.1 kBq/m^3 (**Table 5**), with mean value of 40.2 kBq/m^3. The calculated Rn concentration in the XXFS was higher than the statistically defined anomaly threshold (24.9 kBq/m^3) (**Table 2**). Therefore, the Rn concentrations that exceeded the calculated value were likely not supported by *in-situ* production.

The measurement sites with high Rn concentrations were spatially consistent with the distributions of the volcanic and acidic intrusions in the XXFS (**Figure 5D** and **Table 4**). The abovementioned analysis concluded that the concentrations of Rn lower than the UAT in the XXFS might originate from *in-situ* production. Rn concentrations higher than the UAT in the XXFS might be related to the upward migration of Rn along the

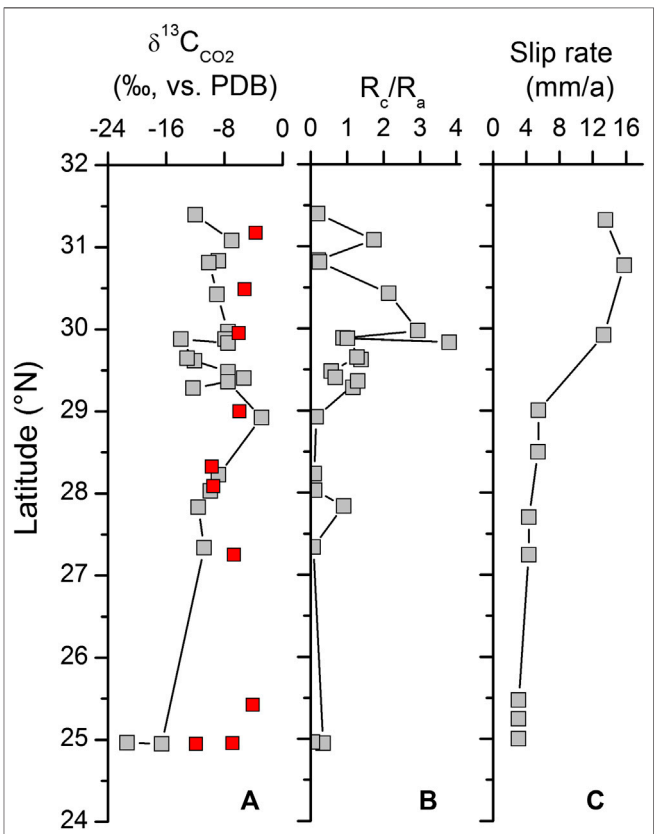

FIGURE 8 | Variations of $\delta^{13}C_{CO2}$ values **(A)**, R_c/R_a ratios **(B)**, and fault slip rates **(C)** from north to south in the XXFS. The colour symbols are data reported in this study. The grey symbols are data reported by previous studies. Data sources: Chen (2006), Shen et al. (2007), Shi et al. (2012), Zhou et al. (2015), and Yue et al. (2017).

TABLE 4 | Strata of the measurement sites in the XXFS.

Measurement site	Strata[a]
M1	Intermediate volcanic rock
M2	Basic volcanic rock
M3	Indosinian intermediate and acidic intrusions
M4	Chengjiangian intermediate and acidic intrusions
M5	(1) yanshanian intermediate and acidic intrusions (2) intermontane depression and fault-subsidence
M6	Multicolored polyterrigenous, red polyterrigenous and molasse formation
M7	Algal-reef carbonate, distal siliceous and endogenous carbonate formation
M8	(1) sandstone, shale and carbonateous shale intercalated with carbonate rock (2) dolomite and limestone intercalated with siltstone and shale
M9	(1) basic volcanic rock (2) dolomite and limestone
M10	Basic volcanic rock

[a]*Data sources: BGMRSP, 1993.*

TABLE 5 | Parameters of radium concentration (C_{Ra}), emanation power coefficient (ε), soil density (ρ), and effective porosity coefficient (n) in the XXFS.

Site	C_{Ra}[a] (Bq/kg)	ε[b]	ρ[c] (kg/m^3)	n[d]	C_{Rn} (kBq/m^3)
M1	36.5	0.48	1,490	0.44	59.3
M2	36.5	0.48	1,140	0.57	35.0
M3	36.5	0.48	1,390	0.48	50.7
M4	36.5	0.48	1,510	0.43	61.5
M5	36.5	0.12	1,350	0.49	12.1
M6	36.5	0.12	1,350	0.49	12.1
M7	36.5	0.074	1,440	0.46	8.5
M8	36.5	0.4	1,500	0.43	50.9
M9	36.5	0.48	1,380	0.48	50.4
M10	36.5	0.48	1,500	0.43	61.1

[a]*Data sources: Sun et al. (2004).*
[b]*Data sources: Righi and Bruzzi (2006); Jobbágy et al. (2009); Qin (2012); Shen et al. (2012).*
[c]*Data sources: the Harmonized World Soil database (HWSD).*
[d]*The soil porosity is calculated by using the formula n = 1-(subsoil bulk density/2.65). The soil density took value of 2.65 g/cm^3, which is the mean density of soil porosity. See details in the text.*

faults. Rn degassing from the fault was also verified by the spatial distributions of Rn concentrations in the XXFS (**Figure 5D**). Additionally, the high concentrations of Rn in M5 (**Figure 5D**) demonstrate the degassing of Rn from the fault according to the field survey.

Relationship Between Soil-Gas Concentration and Fault Activity

In our study, high concentrations of Rn were primarily found at the XSH fault (**Figure 5D** and **Table 1**), which has the highest stress, fault slip rate, and maximum strain rate in the XXFS (**Figure 8C** and Chen., 2006; He and Lu, 2007; Shi et al., 2012; Zhao et al., 2015; Yue et al., 2017; Li et al., 2019). Fault activity can facilitate the transport of fluids due to episodic fracturing events that can release quantities of deep fluids (Evans et al., 1997; Kulongoski et al., 2005; Tanikawa et al., 2010; Zhang et al., 2016).

In our study, granites are well-developed in the XSH fault (BGMRSP, 1993; **Table 4**). In a previous study, the permeability of granites increased by three orders of magnitude as the slip rate increased, indicating that increasing the slip rate could create and maintain elevated fault permeability (Zhang et al., 2017).

From the spatial distributions of soil gases in the XXFS (**Figure 5**), the anomalously high concentrations of CH_4, H_2, CO_2, Rn, and Hg appeared near the fault, which might indicate that the fault slip-rate influenced degassing from the active fault zone. The elevated permeability of the fault facilitates the migration of gases in the active fault zone. The different patterns of soil-gas concentrations across the fault might be influenced by the permeability of the fault zone, such as the porosity of the fault and soil characteristics of the measurement site (e.g. Fu et al., 2005).

CONCLUSION

In this study, the geochemical characteristics of soil gas and the relationship between degassing and fault activity in the XXFS were examined. Summarising:

(1) The mean concentrations of CH_4, H_2, CO_2, Rn, and Hg in the XXFS are 8.1 ppm, 9.9 ppm, 0.5%, 15.1 kBq/m^3, and 12.9 ng/m^3, respectively. Anomalously high concentrations of soil gases primarily appeared near the fault, indicating the degassing of faults in the XXFS.
(2) In the XXFS, the $\delta^{13}C_{CO2}$ and $\delta^{13}C_{CH4}$ values varied from −11.9‰ to -3.7‰ and −62.5‰ to 17‰, respectively. He-C

isotopic analysis indicates that the soil gas in the XSH, ANH, and ZMH faults might have originated from deep fluids, whereas the carbon in the XJ fault is of organic origin. The CH_4 in the XXFS might have thermogenic and abiotic origins.

(3) The concentrations of Rn lower than the UAT in the XXFS might be due to the *in-situ* production. The anomaly of Rn concentrations (higher than the UAT) in the XXFS might be related to the upward migration of Rn along the faults.

(4) The distributions of the high concentrations of soil gases were spatially coincident with the highest stress and the maximum strain rate in the XXFS, which might indicate that the fault activity enhanced permeability and, thus, increased gas emission rates.

DATA AVAILABILITY STATEMENT

The original contributions presented in the study are included in the article/**Supplementary Material**, further inquiries can be directed to the corresponding author.

AUTHOR CONTRIBUTIONS

YS: Methodology, data analysis, conceptualization and writing XZ: Investigation, methodology and conceptualization YY: Investigation JL: Investigation WF: Investigation WW: Investigation YL: Investigation.

FUNDING

This study was supported by the National Key Research and Development Project (2017YFC1500501), the National Natural Science Foundation of China (41673106, 41902312), the Special Fund of the Institute of Earthquake Forecasting, China Earthquake Administration (2017IES010205, 2016IES010304, 2018IES010104, 2020IEF0604, 2020IEF0703) and the Natural Science Foundation of Hebei Province (D2020403050).

ACKNOWLEDGMENTS

The authors are grateful to Fang Du and Hong Fu for their assistance with fieldwork. Two anonymous referees are acknowledged for their extremely constructive reviews of an earlier version of the paper. We thank the journal editor, Francesco Italiano, for his support. Harmonized World Soil Database (HWSD) is thanked for providing the soil data in this research. The CGIAR Consortium for Spatial Information (CGIAR-CSI) provided the STRM data.

SUPPLEMENTARY MATERIAL

The Supplementary Material for this article can be found online at: https://www.frontiersin.org/articles/10.3389/feart.2021.635178/full#supplementary-material.

REFERENCES

Åkerblom, G. (1993). *Ground radon: monitoring procedure in Sweden: lecture at the"JAG" discussion meeting on "radon workshop, Geology, environment, technology"*. London,United Kingdom: Royal Astronomical Society.

Allen, C. R., Luo, Z. L., Qian, H., Wen, X. Z., Zhou, H. W., and Huang, W. S. (1991). Field study of a highly active fault zone: the Xianshuihe fault of southwestern China. *Geol. Soc. Am. Bull.* 103, 1178–1199.

Ball, T. K., Cameron, D. G., Colman, T. B., and Roberts, P. D. (1991). Behaviour of radon in the geological environment: a review. *Q. J. Eng. Geol.y* 24, 169–182.

BGMRSP (1993). *Regional Geology of xizang (Tibet) autonomous region*. Beijing, China: Geological Publishing House.

Bohnhoff, M., and Zoback, M. D. (2010). Oscillation of fluid-filled cracks triggered by degassing of CO_2 due to leakage along wellbores. *J. Geophys. Res.* 115, B11305. doi:10.1029/2010JB000848

Chen, G. (2006). Structural transformation and strain partitioning along the northeast boundary belt of the Sichuan-Yunnan Block. Doctor's Thesis. Beijing (China): Institute of Geology, China Earthquake Administration.

Cheng, W. (1996). Measurement of rhizosphere respiration and organic matter decomposition using natural 13C. *Plant and Soil* 183, 263–268.

Chiodini, G., Cardellini, C., Amato, A., Boschi, E., Caliro, S., Frondini, F., et al. (2004). Carbon dioxide Earth degassing and seismogenesis in central and southern Italy. *Geophys. Res. Lett.* 31, L07615. doi:10.1029/2004GL019480

Ciotoli, G., Bigi, S., Tartarello, C., Sacco, P., Lombardi, S., Ascione, A., et al. (2014). Soil gas distribution in the main coseismic surface rupture zone of the 1980, Ms = 6.9, Irpinia earthquake (southern Italy). *J. Geophys. Res. Solid Earth* 119, 2440–2461. doi:10.1002/2013JB010508

Ciotoli, G., Etiope, G., Marra, F., Florindo, F., Giraudi, C., and Ruggiero, L. (2016). Tiber delta CO_2-CH_4 degassing: a possible hybrid, tectonically active Sediment-Hosted Geothermal System near Rome. *J. Geophys. Res. Solid Earth* 121, 48–69. doi:10.1002/2015JB012557

Di Martino, R. M. R., Capasso, G., and Camarda, M. (2016). Spatial domain analysis of carbon dioxide from soils on Vulcano Island: implications for CO_2 output evaluation. *Chem. Geol.* 444, 59–70. doi:10.1016/j.chemgeo.2016.09.037

Du, J., Si, X., Chen, Y., Fu, H., and Jian, C. (2008). "Geochemical anomalies connected with great earthquakes in China," in *Geochemistry research advances*. Editor Stefánssonó (New York, NY: Nova Science Publishers, 57–92.

Dubois, C., Alvarez Calleja, A., Bassot, S., and Chambaudet, A., (1995). "Modelling the 3-dimensional microfissure network in quartz in a thin section of granite," in *Gas geochemistry*. Editor C. Dubois (Northwood, London: Science Reviews), 357–368.

Einarsson, P., Theodórsson, P., Hjartardóttir, Á. R., and Guðjósson, G. I. (2008). Radon changes associated with the earthquake sequence in June 2000 in the south Iceland seismic zone. *Pure Appl. Geophys.* 1, 63–74. doi:10.1007/s00024-007-0292-6

Evans, J. P., Foster, C. B., and Goddard, J. V. (1997). Permeability of fault-related rocks, and implications for hydraulic structure of fault zones. *J. Struct. Geol.* 19, 1393–1404.

FAO/IIASA/ISRIC/ISSCAS/JRC (2012). *Harmonized World soil Database (version 1.2)*. RomeLaxenburg, Austria: FAO.

Fu, C., Yang, T. F., Walia, V., and Chen, C. (2005). Reconnaissance of soil gas composition over the buried fault and fracture zone in southern Taiwan. *Geochem. J.* 39, 427–439. doi:10.2343/geochemj.39.427

He, J., and Lu, S. (2007). Lower friction of the Xianshuihe–Xiaojiang fault system and its effect on active deformation around the south-eastern Tibetan margin. *Terra Nova* 19, 204–210. doi:10.1111/j.1365-3121.2007.00735.x

Hong, W., Yang, T., Walia, V., Lin, S., Fu, C., Chen, Y., et al. (2010). Nitrogen as the carrier gas for helium emission along an active fault in NW Taiwan. *J. Appl. Geochem.* 25, 593–601. doi:10.1016/j.apgeochem.2010.01.016

Irwin, W. P., and Barnes, I. (1980). Tectonic relations of carbon dioxide discharges and earthquakes. *J. of Geo. Res.* 85, 3115–3121. doi:10.1029/JB085iB06p03115

Javoy, M., Pineau, F., and Delorme, H. (1986). Carbon and nitrogen isotopes in the mantle. *Chem. Geol* 57, 41–62. doi:10.1016/0009-2541(86)90093-8

Jiang, G., Xu, X., Chen, G., Liu, Y., Fukahata, Y., Wang, H., et al. (2014). Geodetic imaging of potential seismogenic asperities on the Xianshuihe-Anninghe-Zemuhe fault system, southwest China, with a new 3-D viscoelastic interseismic coupling model. *J. Geophys. Res. Solid Earth* 120, 1855–1873. doi:10.1002/2014JB011492

Jobbágy, V., Somlai, J., Kovács, J., Szeiler, G., and Kovács, T. (2009). Dependence of radon emanation of red mud bauxite processing wastes on heat treatment. *J. Hazard. Mater* 172, 1258–1263. doi:10.1016/j.jhazmat.2009.07.131

King, C. Y. (1986). Gas geochemistry applied to earthquake prediction: an overview. *J. Geophys. Res. Solid Earth* 91, 12269–12281. doi:10.1029/JB091iB12p12269

Kulongoski, J., Hilton, D., and Izbicki, J. (2005). Source and movement of helium in the eastern Morongo groundwater Basin: the influence of regional tectonics on crustal and mantle helium fluxes. *Geochim. Cosmochim. Acta* 69, 3857–3872. doi:10.1016/j.gca.2005.03.001

Li, Q., Wang, Y., Zhou, Y., and Zhao, C. (2018). Geochemical characteristics of hot spring gases from the Deqing-Zhongdian area, northwestern Yunnan, China. *Bull. Mineral. Petrol. Geochemistry* 37, 645–651. doi:10.19658/j.issn.1007-2802.2018.37.097

Li, Y., Du, J., Wang, F., Zhou, X., Pan, X., and Wei, R. (2009). Geochemical characteristics of soil gas in Yanqing-Huailai basin, North China. *Acta Seismologica Sinica* 31, 82–91.

Li, Y., Liu, M., Li, Y., and Chen, L. (2019). Active crustal deformation in southeastern Tibetan Plateau: the kinematics and dynamics. *Earth Planet. Sci. Lett.* 523, 115708. doi:10.1016/j.epsl.2019.07.010

Liu, G., and Wang, Z. (2020). Correlations of the deep structural characteristics, tidal stress variation and earthquake initiation along the Xianshuihe-Anninghe fault zone. *Chinese J. of Geophy.* 63, 928–943. doi:10.6038/cjg2020N0206

Marty, B., and Jambon, A. (1987). $C/^3He$ in volatile fluxes from the solid Earth: implications for carbon geodynamics. *Earth and Planetary Science Letters* 83, 16–26.

Milkov, A. V., and Etiope, G. (2018). Revised genetic diagrams for natural gases based on a global dataset of >20,000 samples. *Organic Geochemistry* 125, 109–120. doi:10.1016/j.orggeochem.2018.09.002

Morawska, L., and Phillips, C. R. (1993). Dependance of the radon emanation coefficient on radium distribution and internal structure of the material. *Geochimica et Cosmochimica Acta* 57, 1783–1797.

Qin, C. (2012). *Study on distribution and model of soil radon in South China*. Beijing, China: Master degree thesis of China University of Geosciences (Beijing), 1–41.

Ren, Z., Lin, A., and Rao, G. (2010). Late pleistocene–holocene activity of the Zemuhe fault on the southeastern margin of the Tibetan plateau. *Tectonophysics* 495, 324–336. doi:10.1016/j.tecto.2010.09.039

Righi, S., and Bruzzi, L. (2006). Natural radioactivity and radon exhalation in building materials used in Italian dwellings. *J Environ Radioact* 88, 158–170. doi:10.1016/j.jenvrad.2006.01.009

Sano, Y., and Marty, B. (1995). Origin of carbon in fumarolic gas from island arcs. *Chemical Geology* 119, 265–274.

Sciarra, A., Cantucci, B., and Coltorti, M. (2017). Learning from soil gas change and isotopic signatures during 2012 Emilia seismic sequence. *Sci Rep.* 7, 14187. doi:10.1038/s41598-017-14500-y

Sciarra, A., Cantucci, B., Sapia, V., De Ritis, R., Ricci, T., Civico, R., et al. (2020). Geochemical and geoelectrical characterization of the Terre Calde di Medolla (Emilia-Romagna, northern Italy) and relations with 2012 seismic sequence. *J. of Geochemical Exploration* 221, 106688. doi:10.1016/j.gexplo.2020.106678

Sciarra, A., Fascetti, A., Moretti, A., Cantucci, B., Pizzino, L., Lombardi, S., et al. (2015). Geochemical and radiometric profiles through an active fault in the Sila Massif (Calabria, Italy). *J. for Geochemical Exploration* 148, 128–137. doi:10.1016/j.gexplo.2014.08.015

Sciarra, A., Mazzini, A., Inguaggiato, S., Vita, F., Lupi, A., and Hadi, S. (2018). Radon and carbon gas anomalies along the Watukosek fault system and Lusi mud eruption, Indonesia. *Marine and Petroleum Geology* 90, 77–90. doi:10.1016/j.marpetgeo.2017.09.031

Shen, C., Shen, L., Xiao, D., and Tan, Y. (2012). Numerical computation of radon distribution in different soils. *Atomic Energy Science and Technology* 46, 370–374.

Shen, L., Yuan, D., Ding, T., Li, Y., Le, G., and Lin, Y. (2007). Distributing inhomogeneity of helium isotope of CO_2 degasification point and its geotectogenesis in southwest of China. *Acta Geologica Sinica* 81, 475–487.

Shi, F., You, W., and Yun, W. (2012). Recent crustal movement characteristics of Xiaojiang River fault based on the GPS data. *J. of Seismological Research* 35, 207–212.

Sinclair, A. J. (1991). A fundamental approach to threshold estimation in exploration geochemistry: probability plots revisited. *J. of Geochemical Exploration* 41, 1–22. doi:10.1016/0375-6742(91)90071-2

Sinclair, A. J. (1974). Selection of threshold values in geochemical data using probability graphs. *J. Geochem. Explor.* 3, 129–149.

Sun, K., Guo, Q., and Zhuo, W. (2004). Feasibility for mapping radon exhalation rate from soil in China. *J Nucl Sci Technol* 41, 86–90. doi:10.1080/18811248.2004.9715462

Tanikawa, W., Sakaguchi, M., Tadai, O., and Hirose, T. (2010). Influence of fault slip rate on shear-induced permeability. *J. of Geophys. Res.* 115, B07412. doi:10.1029/2009JB007013

Tanner, A. B. (1964). "Radon migration in the ground: a review," in *Natural radiation environment*. Editors J. A. Adams and W. Lowder (Illinois, IL: University of Chicago Press), 161–190.

Tapponnier, P., Zhiqin, X., Roger, F., Meyer, B., Arnaud, N., Wittlinger, G., et al. (2001). Oblique stepwise rise and growth of the Tibet plateau. *Science* 294, 1671–1677. doi:10.1126/science.105978

Toutain, J. P., and Baubron, J. C. (1999). Gas geochemistry and seismotectonics: a review. *Tectonophysics* 304, 1–27.

Walia, V., Lin, S. J., Fu, C. C., Yang, T. F., Hong, W., Wen, H., et al. (2010). Soil–gas monitoring: a tool for fault delineation studies along Hsinhua Fault (Tainan), Southern Taiwan. *J. Appl. Geochem.* 25, 602–607. doi:10.1016/j.apgeochem.2010.01.017

Wang, H., Liu, J., Shi, Y., Zhang, H., and Zhang, G. (2008). Dynamic simulation of interactions between major earthquakes on the Xianshuihe fault zone. *Science in China Series D: Earth Sciences* 51, 1388–1400. doi:10.1007/s11430-008-0110-8

Wen, X., Du, F., Long, F., and Zhu, H. (2011). Tectonic dynamics and correlation of major earthquake sequences of the Xiaojiang and Qujiang-Shiping fault systems, Yunnan, China. *Sci China Earth Sci* 54, 1563–1575. doi:10.1007/s11430-011-4231-0

Williams-Jones, G., Stix, J., Heiligmann, M., Charland, A., Sherwood Lood, B., Arner, N., et al. (2000). A model of diffuse degassing at three subduction-related volcanoes. *Bull. Volcanol.* 62, 130–142. doi:10.1007/S004450000075

Xiang, Y., Sun, X., Liu, D., Yan, L., Wang, B., and Gao, X. (2020). Spatial distribution of Rn, CO_2, Hg, and H_2 concentrations in soil gas across a thrust fault in Xinjiang, China. *Front. Earth Sci.* 8, 554924. doi:10.3389/feart.2020.554924

Yang, T. F., Wen, H., Fu, C., Lee, H., Lan, T., Chen, A., et al. (2011). Soil radon flux and concentrations in hydrothermal area of the tatun volcano group, northern taiwan. *Geochem. J.* 45, 483–490.

Yuce, G., Fu, C. C., D'Alessandro, W., Gulbay, A. H., Lai, C. W., Bellomo, S., et al. (2017). Geochemical characteristics of soil radon and carbon dioxide within the dead sea fault and karasu fault in the mik basin (hatay), Turkey. *Chem. Geol.* 469, 129–146.

Yue, C., Dang, Y., Yang, Q., and Zou, B. (2017). Analysis of the current activity in Sichuan-Yunnan Region and its sub blocks of main faults. *Geod Geodyn.* 37, 176–181.

Zhang, L., Liu, Y., Bao, C., Gao, X., Su, Q., and Fang, Z. (2019b). Characteristics of fault soil gas in Manning of western Sichuan Province, China. *Environmental Chemistry* 38, 777–783. doi:10.7524/j.issn.0254-6108.2018100501

Zhang, L., Liu, Y. W., Bao, C., and Guo, L. S. (2019a). Distribution characteristics of soil mercury in Anninghe fault zone. *Acta Seismologica Sinica* 41, 249–258. doi:10.11939/jass.20180141

Zhang, M., Guo, Z., Zhang, L., Sun, Y., and Cheng, Z. (2017). Geochemical constraints on origin of hydrothermal volatiles from southern Tibet and the Himalayas: understanding the degassing systems in the India-Asia continental subduction zone. *Chemical Geology* 469, 19–33. doi:10.1016/j.chemgeo.2017.02.023

Zhang, W., Du, J., Zhou, X., and Wang, F. (2016). Mantle volatiles in spring gases in the Basin and Range Province on the west of Beijing, China: constraints from

helium and carbon isotopes. *J Volcanol Geotherm Res.* 309, 45–52. doi:10.1016/j.jvolgeores.2015.10.024

Zhao, J., Jiang, Z. S., Niu, A. F., Liu, J., Wu, Y. Q., Wei, W. X., et al. (2015). Study on dynamic characteristics of fault locking and fault slip deficit in the eastern boundary of the Sichuan-Yunnan rhombic block. *Chinese J. of Geophy.* 58, 872–885. doi:10.6038/cjg20150316

Zhou, X., Chen, Z., and Cui, Y. (2016). Environmental impact of CO_2, Rn, Hg degassing from the rupture zones produced by Wenchuan M s 8.0 earthquake in western Sichuan, China. *Environ Geochem Health* 38, 1067. doi:10.1007/s10653-015-9773-1

Zhou, X., Du, J., Chen, Z., Cheng, J., Tang, Y. L., et al. (2010). Geochemistry of soil gas in the seismic fault zone produced by the Wenchuan Ms 8.0 earthquake, southwestern China. *Geochem Trans* 11, 5. doi:10.1186/1467-4866-11-5

Zhou, X. C., Sun, F. X., Chen, Z., Lv, C. J., Li, J., Wu, K. T., et al. (2017). Degassing of CO_2, CH_4, Rn, and Hg in the rupture zones produced by Wenchuan Ms 8.0 earthquake. *Acta Petrologica Sinica* 33, 291–303.

Zhou, X. C., Wang, W. L., Li, L. W., Hou, J. M., Xing, L. T., Li, Z. P., et al. (2020). Geochemical features of hot spring gases in the Jinshajiang-Red River fault zone, Southeast Tibetan Plateau. *Acta Petrologica Sinica* 36, 2197–2214. doi:10.18654/1000-0569/2020.07.18

Zhou, X., Wang, W., Chen, Z., Li, Y., Liu, L., Xie, C., et al. (2015). Hot spring gas geochemistry in western sichuan Province, China after the wenchuan ms 8.0 earthquake. *Terrestrial Atmospheric and Oceanic Sciences* 26, 361–373.

Conflict of Interest: The authors declare that the research was conducted in the absence of any commercial or financial relationships that could be construed as a potential conflict of interest.